Advanced Materials

ADVANCED MATERIALS
www.advmat.de

RESEARCH ARTICLE

Dual-Functional Fluorinated Additive in Gel Polymer Electrolyte for High-Energy-Density Anode-Free Lithium Batteries With Enhanced Thermal Stability

Shengyu Cong[1] | Zhenghao Yang[1] | Han Chen[1] | Xuhao Wan[2] | Myeong Gyun Nam[1] | Tong Wang[3] | Sheng Zhang[3] | Maya Narayanan Nair[3] | Yuanyuan Ma[4] | Yang Li[4] | Hyunsik Woo[5] | Seung Woo Lee[5] | Yongseok Kim[4] | Yuzheng Guo[6] | Yuan Yang[1]

[1]Department of Applied Physics and Applied Mathematics, Columbia University, New York, New York, USA | [2]Center for Materials Theory, Department of Physics and Astronomy, Rutgers University, Piscataway, New Jersey, USA | [3]Advanced Science Research Center at the Graduate Center, City University of New York, New York, New York, USA | [4]Samsung SDI R&D America (SDIRA), Cambridge, Massachusetts, USA | [5]Next Generation Development Group, Samsung SDI Research Center, Suwon-si, Gyeonggi-do, Republic of Korea | [6]School of Electrical Engineering and Automation, Wuhan University, Wuhan, China

Correspondence: Yuzheng Guo (yguo@whu.edu.cn) | Yuan Yang (yy2664@columbia.edu)

Received: 19 February 2026 | **Revised:** 27 May 2026 | **Accepted:** 30 June 2026

Keywords: chemical engineering | electrochemistry | electrolyte | flammability | fluorine | materials science | polymer | thermal runaway | thermal stability

ABSTRACT

Anode-free lithium metal batteries offer high energy density and low cost, but their practical deployment is limited by unstable lithium–electrolyte interfaces and safety risks from dendrite growth and flammable electrolytes. Here, we report a dual-functional fluorinated additive that enables in situ gelation, forming a thin, inorganic-rich solid electrolyte interphase while simultaneously enhancing flame retardancy through radical capture. At 0.5 C discharge, the additive-enabled anode-free pouch cell delivers high specific capacities of 202.1 mAh/g (3.0–4.5 V) and 192.0 mAh/g (3.4–4.3 V), while retaining 80.3% and 80.1% of their initial values after 85 and 100 cycles, respectively. Moreover, Cu/NCA pouch cells with capacities of 1.4 Ah (3.0–4.5 V) and 200 mAh (3.6–4.3 V), incorporating the additive, retain 80.2% of initial capacity after 85 cycles and 92.9% after 100 cycles, respectively. Such performance is on par with or better than the best results in the literature. Impressively, such a 1.4 Ah cell shows no thermal runaway in a harsh drilling test at the fully charged state, even after 100 cycles. These results demonstrate that the dual-functional fluorine additive leads to both excellent electrochemical performance and enhanced safety, paving the way for the safe and practical application of anode-free lithium metal cells.

1 | Introduction

Anode-free lithium metal batteries (LMBs) are promising next-generation energy storage systems owing to their high energy density and simplified manufacturing [1–3]. Unlike conventional LMBs, anode-free lithium batteries rely on in situ lithium deposition on the current collector during the first charging, thus maximizing active material utilization and minimizing inactive components [4–6]. For example, anode-free cells employing $LiNi_{1-x-y}Co_xAl_yO_2$ (NCA) cathode show both higher specific energy and energy density than the corresponding lithium-ion batteries (LIBs) and conventional LMBs (Figure 1a and Table S1). Despite these advantages, anode-free LMBs face two key challenges: (i) limited cycle life caused by inhomogeneous lithium deposition and an unstable lithium–electrolyte interface [7], and (ii) safety risks arising from the inhomogeneity of lithium deposition and the flammability of liquid electrolytes [8, 9].

To date, several strategies have been reported to enhance deposition smoothness and stabilize the electrolyte/electrode interface,

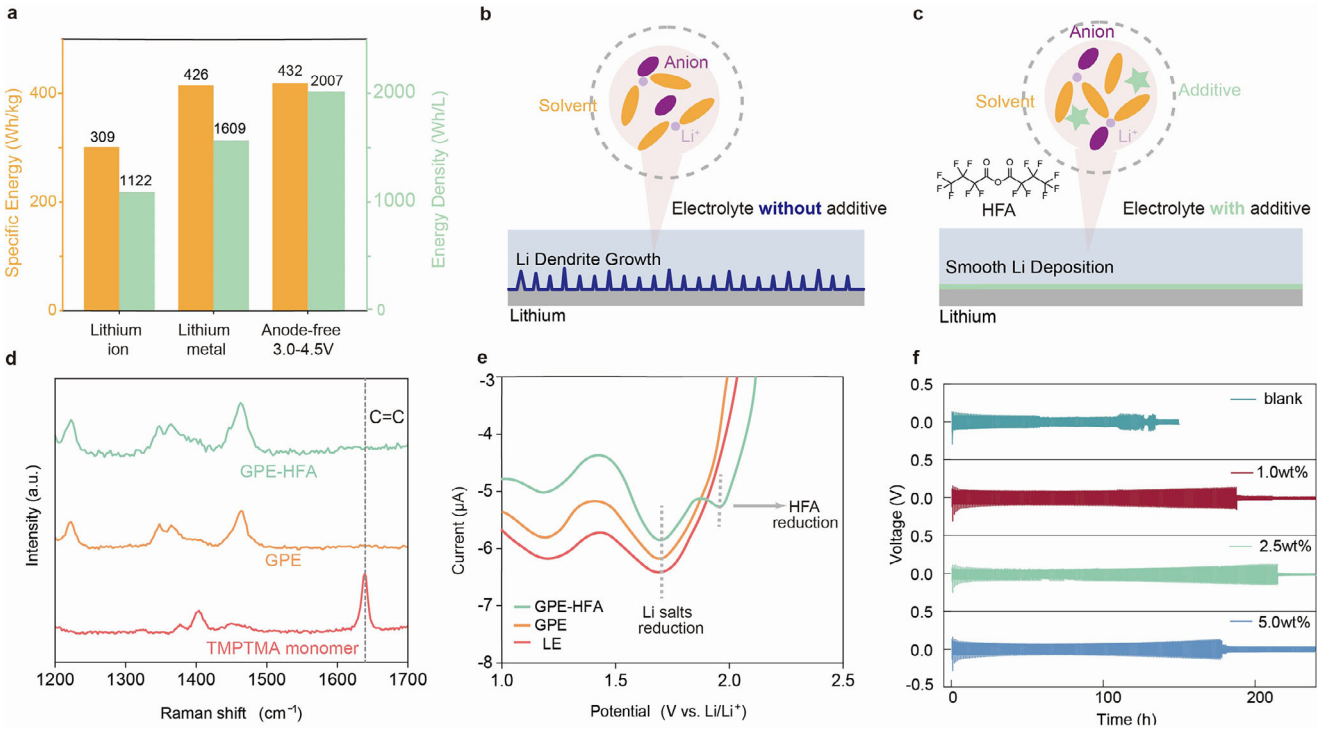

FIGURE 1 | (a) Calculated energy density and specific energy of graphite/NCA, Li/NCA, and Cu/NCA anode-free batteries. Calculation details are in section Table S1. (b) Without additives, Li deposition on a Cu substrate is associated with needle-shaped Li growth and unstable SEI in anode-free cells. Li dendrites grow aggressively, and the SEI layer is highly inhomogeneous. (c) With the HFA additive proposed in this work, uniformly deposited Li with an inorganic-rich SEI layer, which can successfully inhibit the decomposition of organic solvent and suppress Li dendrite growth. (d) Raman spectra analysis of GPE and GPE-HFA after gelation. (e), Electrochemical reduction curves of Li||Cu half-cells using LE, GPE and GPE-HFA at 0.1 mV/s. (f) Li || Li symmetric cell cycling performance with different concentrations of 0, 1.0, 2.5, and 5.0 wt.% HFA additive at a current density of 1.0 mA/cm^2 with a capacity of 0.5 mAh/cm^2.

including electrolyte formulation [10–12], solid-state electrolytes [13, 14], structured anode [15, 16], and optimized charging protocols [17]. Among them, constructing an inorganic-rich (e.g., LiF/Li_2O) solid-electrolyte interphase (SEI) is a promising approach [18, 19]. Owing to the high lithiophobicity, chemical stability, and low Li^+ diffusion barrier, such an inorganic-rich SEI substantially improves the uniformity of lithium plating/stripping [20–22]. High-concentration electrolytes (HCEs) [23] and localized high-concentration electrolytes (LHCEs) [24] can promote an inorganic-rich SEI; however, their practical deployment is hindered by high cost and increased electrolyte density [25, 26]. These drawbacks arise from the excessive salt content in HCEs and the large fractions of heavy fluorinated diluents required in LHCEs (>60 wt.%), which are particularly concerns for large-scale applications where both cost and gravimetric energy density are critical [27, 28]. Besides, HCEs and LHCEs also have safety concerns [29, 30]. Introducing a low concentration of a fluorine-containing additive (<5 wt.%, denoted as F-additive) that favors inorganic-rich SEI formation provides a more cost-effective and scalable approach [31, 32]. An ideal F-additive should combine the following key features: (i) a low lowest unoccupied molecular orbital (LUMO) energy to enable rapid reduction and SEI formation during initial cycles, and (ii) a high F/C molar ratio to preferentially form an inorganic-rich SEI and stabilize the interface. Designing F-additives that meet all these criteria remains a challenge.

In addition, safety remains a critical issue in anode-free batteries because of the flammability of the electrolyte and the parasitic reactions at the anode/electrolyte interface [33]. Gel polymer electrolytes (GPEs) offer a promising pathway toward practical applications. Compared to liquid electrolytes (LEs), GPEs possess high thermal stability and improved electrochemical stability [34]. Moreover, their fabrication via in situ polymerization is readily compatible with existing battery manufacturing processes [35, 36]. In addition, it is desirable for the additive to act as a fire-suppressing or fire-retarding agent to further enhance the cell's thermal stability.

To achieve the safety and cycle-life goals for anode-free cells, we developed a dual-functional fluorinated additive, heptafluorobutyric anhydride (HFA), that enables a gel polymer electrolyte. Owing to its low LUMO and high fluorine content, HFA forms an inorganic-rich interphase (Figure 1c), enabling more stable lithium plating/stripping (Figure 1b) and thereby significantly extending the cycle life. In this work, an HFA-incorporated anode-free pouch cell with a high-loading NCA cathode (4.8 mAh/cm^2) delivers discharge capacities of 202.1 mAh/g (3.0–4.5 V) and 192.0 mAh/g (3.4–4.3 V), while retaining 80.3% and 80.1% of its initial capacity after 85 and 100 cycles, respectively, at a charge/discharge rate of 0.2 C/0.5 C. Furthermore, anode-free pouch cells incorporating HFA, with capacities of 1.4 Ah (3.0–4.5 V) and 200 mAh (3.6–4.3 V), exhibit capacity retentions of 80.2% after 85 cycles and 92.9%

after 100 cycles, respectively, when cycled at 0.2 C/0.5 C charging/discharging under the lean electrolyte condition (2.8 g/Ah) and a low stack pressure of 0.7 MPa. Such performance is on par with, or superior to, the best results reported so far [37–50].

Moreover, HFA enhances the thermal stability of the electrolyte by acting as a gas-phase radical scavenger, providing intrinsic flame-retardant properties that are critical for safe battery operation, especially for high-energy-density lithium metal batteries. Remarkably, a fully charged 200 mAh Cu/NCA pouch cell with HFA additive passes the harsh drilling test, while the HFA-free counterpart 200 mAh cell explodes during drilling. More impressively, at full charge after 100 cycles, the 1.4 Ah anode-free cell shows no thermal runaway under the same drilling test. It should be pointed out that passing the drilling test after 100 cycles is far more difficult than after the first cycle, which is often reported in the literature, since the inhomogeneous lithium deposition after many cycles could accelerate side reactions and thermal runaway [51, 52]. These results highlight the potential of the HFA-based gel electrolyte for safe and practical anode-free energy storage.

2 | Results and Discussion

2.1 | Design Principle of Additive-Enhanced Gel Polymer Electrolyte

Trimethylolpropane trimethacrylate (TMPTMA) is employed as the cross-linker, as it effectively transforms the liquid electrolyte into a gel polymer electrolyte at a low concentration (e.g., 3%–5%), without compromising ionic conductivity [53]. The liquid electrolyte (LE) phase is composed of 1.0 M LiDFOB and 0.4 M $LiBF_4$ in diethyl carbonate (DEC)/fluoroethylene carbonate (FEC) (2:1 by volume), as this formulation delivers one of the highest-performing anode-free batteries [54]. The dual-salt LiDFOB/$LiBF_4$ synergistically regulates interphase chemistry to form a stable SEI, thereby enabling dense dendrite-free lithium deposition and highly reversible lithium plating/stripping [2, 54, 55].

The introduction of HFA could further optimize the SEI composition owing to its lower LUMO energy and preferential reduction during initial cycling [56]. Moreover, HFA acts as a gas-phase radical scavenger, thereby enhancing the thermal stability of the gel electrolyte. An inverted-vial test (Figure S1) shows that only 4 wt.% cross-linker is sufficient to convert the liquid electrolyte into a stable, fully gelled state without observable leakage, as demonstrated by both GPE and GPE-HFA (containing 2.5 wt.% HFA). Further, in both gel electrolytes, Raman spectroscopy reveals the disappearance of the C═C stretching peak at ~1640 cm^{-1} after gallization at 55°C, confirming the complete polymerization of the gel matrix (Figure 1d) [57].

To verify the preferential reduction of HFA at the anode interface, density functional theory (DFT) calculations were performed. As shown in Figure S2, HFA exhibits a significantly lower LUMO energy level (−3.15 eV) compared to DEC (0.06 eV), FEC (−0.37 eV), and TMPTMA (−1.67 eV). This LUMO offset indicates that HFA is thermodynamically more favorable for reduction on the lithium metal surface [58], contributing to the formation of an inorganic-rich SEI and inhibiting solvent consumption. Moreover, the electrochemical window of the electrolytes was tested. As shown in Figure 1e, with the addition of 2.5wt.% HFA, the electrolyte shows an earlier reduction peak (~1.9 V vs. Li^+/Li) than LiDFOB-$LiBF_4$ salts (1.7 V vs. Li^+/Li) [59], providing strong experimental evidence that HFA is preferentially reduced at the electrode surface, in agreement with the DFT calculations.

2.2 | Properties of Gel Polymer Electrolyte

First, to optimize the concentration of HFA in GPE, the GPE (4 wt.% TMPTMA + 96 wt.% LE) with 0, 1.0, 2.5, and 5.0 wt.% HFA additive is tested using Li || Li symmetric coin cells. In Figure 1f, the voltage polarization of the cell without HFA additive begins to increase substantially after 130 h, followed by a short circuit, indicating that lithium dendrites puncture the separator. With 1.0, 2.5, and 5.0 wt.% HFA, the short circuit occurred after 190, 220, and 180 h, respectively. The optimized performance at 2.5 wt.% HFA arises from a balance between interfacial stabilization and Li^+ transport. Low HFA contents (1.0–2.5 wt.%) maintain ionic conductivities close to the baseline electrolyte (2.9 mS/cm), whereas excessive HFA (5.0 wt.%) reduces ionic conductivity to 2.5 mS/cm due to the weak Li^+ transport capability of fluorine-rich HFA molecules (Figure S3). Consistently, 2.5 wt.% HFA delivers the lowest anode charge-transfer resistance, confirming its optimal balance between robust interface formation and efficient ion transport (Figure S4). Therefore, we selected the formulation containing 96 wt.% LE + 4 wt.% TMPTMA as the reference GPE and added 2.5 wt.% HFA to it (denoted GPE-HFA) as the target electrolyte for investigation.

At 25°C, GPE and GPE-HFA exhibit comparable ionic conductivities (2.9 mS/cm), slightly lower than that of LE (3.5 mS/cm). Across 35°C–55°C, both gel electrolytes retain ~80% of the conductivity of LE, indicating that the in situ gelation process does not significantly compromise ionic transport (Figure S5). Besides, the Li^+ transference numbers (t_{Li+}), measured by the Bruce–Vincent–Evans method [60], are 0.35 for LE, 0.30 for GPE, and 0.43 for GPE-HFA (Figure S6). The higher t_{Li+} of GPE-HFA indicates improved Li^+ transport, which stabilizes Li deposition during cycling. GPE-HFA also exhibits excellent electrochemical stability, as confirmed by linear sweep voltammetry (LSV). Specifically, GPE-HFA shows the highest oxidation onset voltage of 5.45 V vs. Li^+/Li, indicating its superior anodic stability (Figure S7).

2.3 | Electrochemical Performance of Anode-Free Cells With the HFA Additive

To systematically understand the effect of the HFA additive on electrochemical performance, we first measured the charge transfer resistance (R_{ct}) in Cu/NCA pouch cells with LE, GPE, GPE-HFA, respectively (Figure 2a,b and Figure S8). The solid lines in Figure 2a show the measured data, and dashed lines correspond to the fitted values. After 50 cycles, the GPE-HFA cell exhibits a reduced $R_{ct\ anode}$ of 1.50 Ω, compared with 2.03 Ω for the GPE cell and 1.72 Ω for the LE, suggesting more efficient interfacial ion transport facilitated by a superior SEI formed in the presence of HFA. This improvement in interfacial kinetics

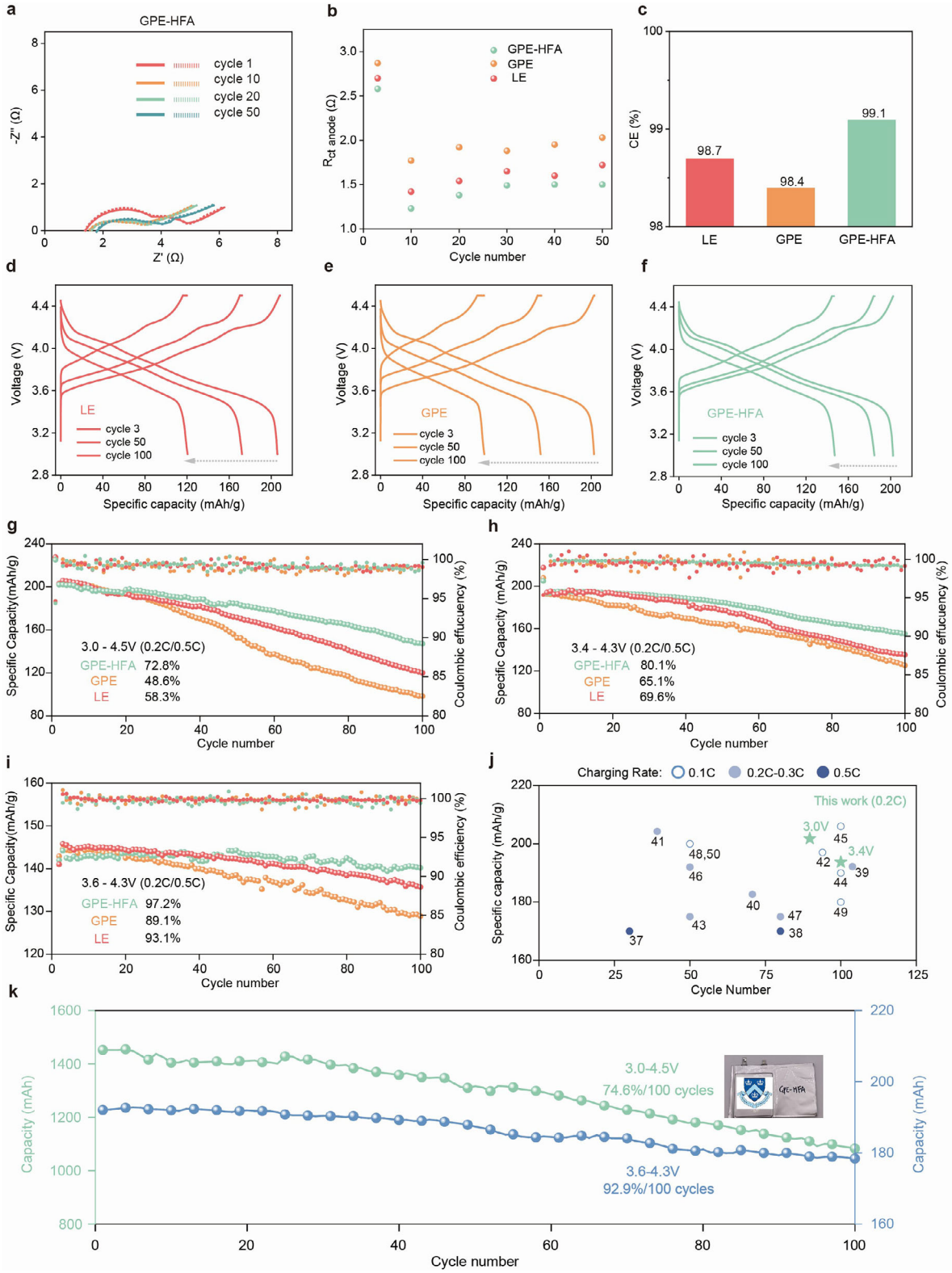

FIGURE 2 | (a) Electrochemical impedance spectra of Cu/GPE-HFA/NCA pouch cells after cycling 50 cycles. (b) The summary of EIS fitting results for reported electrolytes. The lowest $R_{ct\ anode}$ is found in GPE-HFA after 50 cycles. (c) Coulombic efficiency (CE) in Li/Cu half cells. GPE-HFA shows the highest CE among the three electrolytes. (d–f) Voltage profiles of LE-, GPE- and GPE-HFA-based cells (3.0–4.5 V). (g–i) Cycling performance and CE of pouch cells at different voltage windows (0.2C charge/0.5C discharge): g) 3.0–4.5 V; h) 3.4–4.3 V; and i) 3.6–4.3 V. (j) Comparison of discharge specific capacity vs. cycle number (80% retention as cut-off) with best results in literature. Benchmark comparison showing that this work outperforms previous reports at 0.5 C and remains comparable to state-of-the-art performance at lower charging rates (0.2 C and 0.1 C). (k) Cycling performance of the Cu/NCA pouch cells using the GPE-HFA between 3.0–4.5 V (1.4 Ah) and 3.6–4.3 V (200 mAh) after 0.1C formation with a lean electrolyte 2.8 g/Ah at 0.2C charge/0.5C discharge, showing impressive performance.

is further corroborated by the enhanced Coulombic efficiency (CE) measured in Li/Cu half-cells. As shown in Figure S9, the nucleation overpotential decreases from 382 mV in the GPE to 230 mV in the GPE-HFA, indicating the formation of a highly Li^+-conductive SEI that facilitates more uniform lithium nucleation and growth [61]. Following the standard Aurbach protocol [62, 63], the GPE-HFA achieved a high CE of 99.1%, surpassing that of the GPE counterpart (98.4%) and LE (98.7%) in Li/Cu half cells (Figure 2c). This superior CE highlights the excellent reversibility of lithium plating/stripping in the presence of the HFA additive, which is essential for long-term cycling stability in anode-free configurations.

The reduced $R_{ct\ anode}$, and enhanced CE in GPE-HFA further contribute to improved cycling performance in full cells. We assembled Cu/NCA single-layer pouch cells with a cathode ($1.8 \times 1.8\ cm^2$) loading of 4.8 mAh/cm^2, an electrolyte amount of 6 g/Ah, and a uniaxial stack pressure of 0.7 MPa (Figure S10). Commercial Cu foil was used as received, without further treatment. After a formation step at 0.1 C, the cells were cycled at 0.2 C charge and 0.5 C discharge (1 C = 4.8 mA/cm^2). Three voltage windows were selected to probe different operating regimes: 3.0–4.5 V for maximum capacity and stability limits, 3.4–4.3 V for balanced energy density and cycling stability, and 3.6–4.3 V for a practically relevant condition defined based on energy density considerations (see Table S2 and Figure S11 for details).

Within a voltage window of 3.0–4.5 V, GPE-HFA exhibits more stable cycling than LE and GPE (Figure 2d–f). The initial discharge capacity at 0.1 C reached 227 mAh/g. At a higher discharge rate of 0.5 C, the discharge capacities decreased to 205.8, 202.3, and 202.1 mAh/g for LE, GPE, and GPE-HFA, respectively, reflecting the typical capacity reduction associated with kinetic limitations at elevated current densities [64]. After 85 cycles, GPE-HFA maintained 80.3% of the initial capacity, significantly outperforming GPE (54.5%) and the liquid electrolyte (65.7%) (Figure 2g). Even after 100 cycles, GPE–HFA still delivers an impressive capacity retention of 72.8%.

At an elevated cycling rate of 0.3 C charge/1.0 C discharge, the GPE-HFA cell retained 70.5% of its capacity after 100 cycles, outperforming the GPE (46.2%) and LE (56.8%) cells (Figures S12 and S13), indicating improved interfacial stability and charge-transfer kinetics under high-current operation. Rate-capability tests further show that GPE-HFA delivers more stable capacities at increasing discharge rates from 0.5 to 2.0 C and recovers well when the rate returns to 0.5 C, confirming its enhanced rate performance and cycling reversibility (Figure S14).

Furthermore, within a voltage window of 3.4–4.3 V at 0.5 C, GPE-HFA achieves a high initial specific capacity of 192.0 mAh/g, and retains 80.1% of its capacity after 100 cycles, markedly surpassing GPE (65.1%) and the LE (69.6%) (Figure 2h and Figure S15). In addition, a cut-off voltage of 3.6 V was selected because calculations show that in the voltage range of 3.6–4.3 V, the NCA/Cu cell can still deliver 36.3% higher volumetric and 6.3% higher specific energy densities than a commercial LIB operating between 3.0–4.3 V (Figure S11 and Table S2). As shown in Figure 2i and Figure S16, when cycled at 3.6–4.3 V, the GPE-HFA–based cell delivers a capacity of 144.2 mAh/g and retains 97.2% after 100 cycles, outperforming both GPE (89.1%) and LE (93.1%). The cycling performance with different voltage cut-offs is summarized in Tables S3 and S4.

Besides better cycling retention, GPE-HFA also exhibits higher conductivity retention and lower electrolyte leakage. After 100 cycles, LE, GPE, and GPE-HFA retain 77% (2.7 mS/cm), 69% (2.0 mS/cm), and 86% (2.5 mS/cm) of their initial ionic conductivities, respectively (Figure S17). The much better conductivity retention for GPE-HFA indicates better preserved ion-transport pathways and suppressed interfacial/electrolyte degradation during cycling. In the leakage current test (Figure S18), GPE-HFA delivers a lower leakage current (0.08 mA/g) than LE (0.20 mA/g) and GPE (0.15 mA/g), indicating suppressed parasitic reactions at 4.5 V.

Overall, these results demonstrate the superior cycling stability of GPE-HFA and highlight the effectiveness of HFA as an additive in polymer electrolyte design for achieving long-term anode-free operation. As shown in Figure S19 and Table S5, the cycling performance achieved in this work exceeds that of previously reported gel-based systems [65–67]. Moreover, to the best of our knowledge, the performance of our gel system is comparable to that of state-of-the-art liquid electrolyte–based systems charged at 0.2 C and 0.1 C reported to date (Figure 2j and Table S6). Notably, achieving such performance at 0.2 C is particularly significant, as lower charging rates (0.1C) typically lead to substantially improved performance [68].

We also evaluated the cycling performance of the GPE-HFA-based 200 mAh and 1.4 Ah multilayer pouch cell. The NCA loading is 3.1 mAh/cm^2, and the electrolyte amount is only 2.8 g/Ah. For the 200 mAh cell, GPE-HFA delivers an initial discharge capacity of 150.6 mAh/g (192.0 mAh) at 0.5 C and retains 92.9% of its capacity after 100 cycles within 3.6–4.3 V (Figure 2k). Notably, within 3.0–4.5V, a 1.4 Ah Cu/NCA pouch cell with GPE-HFA reaches 202.4 mAh/g at 0.5 C, and the capacity remains 80.2% (74.6%) after 85 (100) cycles at a pressure of 0.7 MPa (Figure 2k). The cycling results of large pouch cells highlight the significant benefits of the dual-functional additive HFA for delivering high-performance anode-free lithium metal batteries.

2.4 | Characterization of SEI and Lithium Anode

To further gain a deep insight into the influence of the HFA additive on SEI composition, cryogenic transmission electron microscopy (cryo-TEM) and X-ray photoelectron spectroscopy (XPS) were employed to elucidate the morphological features and chemical compositions of the SEI. Cryo-TEM images reveal that the GPE forms a thick SEI layer of approximately 15 nm (Figure 3a and Figure S20), whereas the GPE-HFA and LE exhibit a thinner SEI of only 8 nm (Figure 3c and Figure S21). This reduced SEI thickness minimizes active lithium ion consumption during each cycle, thereby substantially improving the Coulombic efficiency, which is in agreement with the higher CE observed in GPE-HFA (Figure 2c). Furthermore, high-resolution imaging reveals that the surface layer is crystalline Li_2O, as evidenced by a lattice spacing of 2.68 Å corresponding to the (111) plane of Li_2O (Figure 3b,d). Electron diffraction (ED) patterns further corroborate this assignment, exhibiting

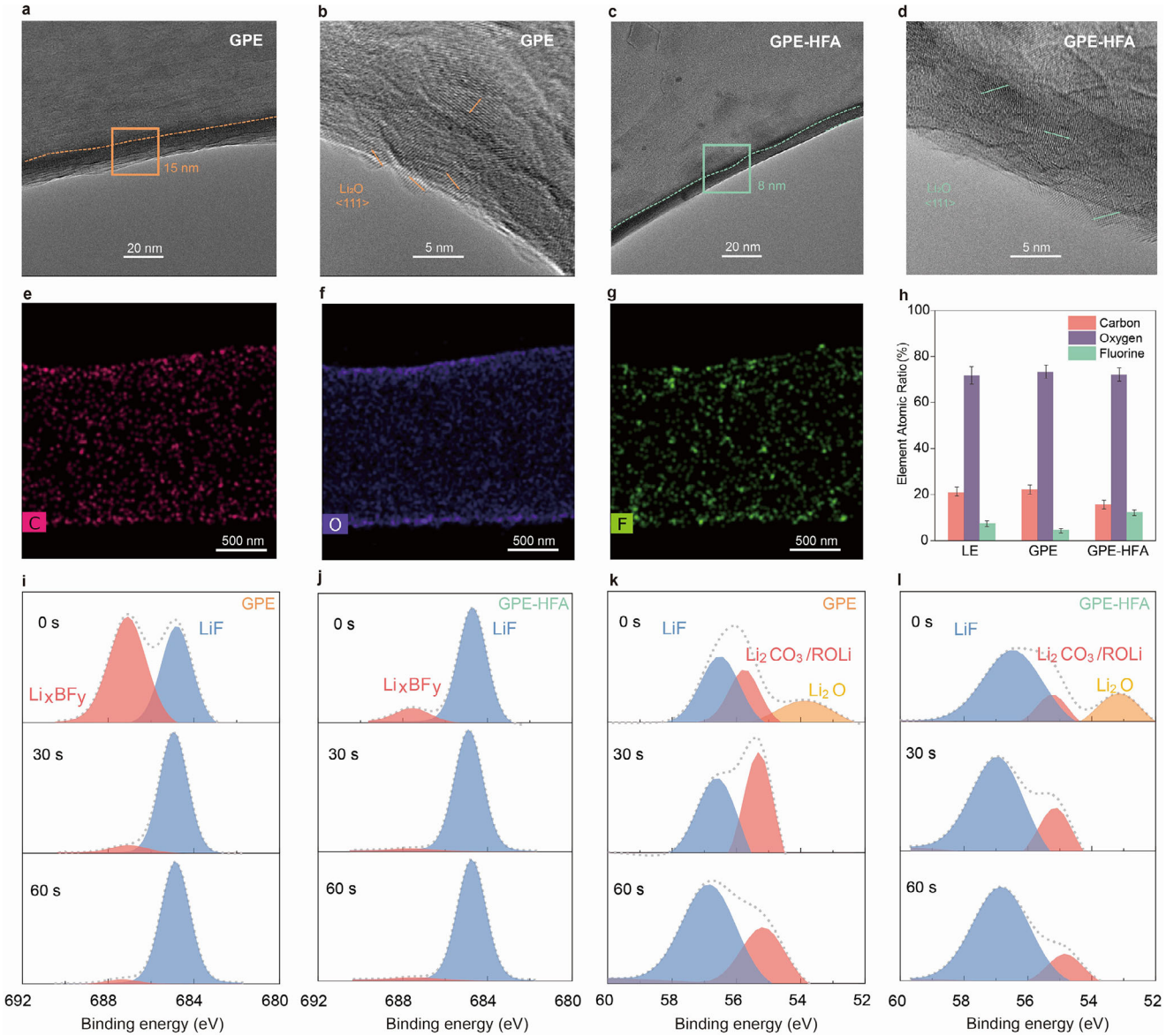

FIGURE 3 | SEI composition characterizations. (a,c), Cryo-TEM image of the SEI layer on lithium metal deposited from GPE and GPE-HFA, respectively. (b,d), Atomic-resolution image of the region outlined in a) and c) showing the structure of the SEI layer. The lattice spacing of small crystalline grains matches that of Li_2O. (e) Carbon, (f) Oxygen, and (g) Fluorine EDS elemental mapping of as-deposited lithium metal. (h) Atomic percentage of carbon, oxygen, and fluorine elements in SEI on lithium metal in cells. In-depth F 1*s* XPS spectra of Li metal anodes after three cycles in (i), GPE, and (j), GPE-HFA. In-depth Li 1*s* XPS spectra of Li metal anodes after three cycles in (k), GPE, and (l), GPE-HFA.

distinct Friedel pairs from the Li metal (110) plane together with polycrystalline rings attributable to Li_2O (111). Notably, no discernible diffraction features associated with LiF are observed. This absence of LiF echoes recent cryogenic electron microscopy studies, which indicate that LiF in compact SEI layers frequently lacks long-range crystallinity and preferentially coexists with Li_2O in an amorphous or nanocomposite form, thus eluding direct lattice-level detection by high-resolution TEM or ED [69, 70].

Complementary energy-dispersive X-ray spectroscopy (EDS) provides further evidence for the presence of fluorine-containing species, revealing fluorine-rich domains (~50–100 nm) on the lithium surface (Figure 3e–g). Quantitatively, the SEI formed with GPE–HFA exhibits a higher fluorine content (12.2%) than those formed with LE (7.5%) and GPE (4.6%) (Figure 3h). Together, these results indicate the formation of an inorganic-rich interphase featuring coexisting Li_2O and LiF species, consistent with our design strategy whereby the HFA additive promotes a robust inorganic-rich SEI.

To further elucidate the chemical composition of the SEI, XPS depth profiling was performed on the lithium metal surface by fabricating Cu/NCA pouch cells after three cycles. As shown in the F *1s* spectra (Figure 3i,j and Figure S22), GPE-HFA shows a dominant LiF peak at 684.7 eV with an atomic concentration of 87.6% on the SEI surface, significantly higher than the 44.2% observed in GPE and 81.5% in LE. This result demonstrates that the incorporation of HFA effectively promotes the formation of a LiF-rich SEI, which is crucial for enhancing long-term

cycling stability. These results further verify that HFA is significantly involved in the formation of SEI. A similar trend is observed in the Li *1s* spectra (Figure 3k,l and Figure S23), where GPE-HFA displays stronger LiF-and Li_2O-related signals. In addition, the characteristic peaks in the C *1s* spectra associated with carbonate-based solvent decomposition [71] are weaker in GPE-HFA (Figure S24), indicating suppressed solvent degradation, which is attributed to the formation of an HFA-enabled, inorganic-rich SEI. B *1s* XPS spectra reveal the presence of Li-B-F and Li-B-O species (Figure S25), indicating that the reductive decomposition of LiDFOB and $LiBF_4$ contributes to the formation of borate-containing inorganic SEI components [72].

Furthermore, the cathode electrolyte interphase (CEI) was investigated after 100 cycles. Cryo-TEM analysis reveals comparable CEI thicknesses (~25 nm) on cycled NCA cathodes for LE, GPE, and GPE-HFA after 100 cycles (Figure S26). Consistently, XPS depth profiling shows similar CEI compositions among the three electrolytes, mainly composed of Li-B-F/Li-B-O species, carbonate-derived components, and LiF (Figures S27–S29). These results indicate that HFA does not substantially alter the cathode-side CEI chemistry. Instead, its primary role is to regulate the anode-side SEI by promoting rapid formation of a compact inorganic-rich interphase, thereby suppressing parasitic reactions and improving cycling stability.

SEM and focused ion beam-scanning electron microscopy (FIB-SEM) characterization further show that the HFA-derived SEI in GPE-HFA leads to better lithium metal morphology compared to LE and GPE. As shown in Figure 4a,b and Figure S30, after three cycles, the LE and GPE both result in a defective Li morphology characterized by a high density of cracks and fragmented grains. Such morphology accelerates electrolyte consumption, depletes the lithium metal anode, and aggravates parasitic side reactions, ultimately degrading the overall electrochemical performance of the battery. In contrast, the GPE-HFA leads to a significantly smoother Li surface with larger and more uniform grains, which confirms the strong ability of HFA-derived SEI to inhibit the growth of Li dendrites and promote homogeneous lithium nucleation and deposition. The uniform and compact lithium deposition morphology achieved with GPE-HFA offers significant advantages by reducing the surface area available for continuous SEI growth and effectively suppressing the formation of inactive lithium, thus promoting cycling life. Notably, the average domain size of deposited lithium in the GPE-HFA system reaches 30.8 μm^2 (Figure 4d), much higher than that observed in the GPE (17.1 μm^2, Figure 4d) and LE (26.2 μm^2, Figure 4e and Figure S31). As shown in Figure 4c, even after 50 cycles, the GPE-HFA cell maintains a more compact lithium morphology than GPE and LE (Figure S32), further confirming the durable stabilization effect of the inorganic-rich SEI induced by the HFA additive.

In addition to forming large lithium domains, GPE-HFA also promotes densely packed lithium deposition, as evidenced by FIB-SEM cross-sectional images. After charging in the 3rd and 50th cycles, the lithium deposition densities in GPE-HFA reach 0.50 and 0.44g/cm^3, respectively, both exceeding the corresponding values observed in the LE (0.49/0.41 g/cm^3) and GPE (0.47/0.40 g/cm^3) systems (Figure 4f,g, and Figures S33 and S34). This increased lithium density in GPE-HFA effectively reduces the electrochemically active surface area exposed to the electrolyte, thus mitigating parasitic side reactions and conserving both electrolyte and active lithium, which is essential for achieving long-term cycling stability. Importantly, the larger lithium deposition domain size and increased metal density observed in GPE-HFA play a key role in suppressing parasitic reactions between lithium and the electrolyte, factors that are critical for achieving long-term cycling stability. As shown in Figure S35, an increased LiF content correlates with the formation of larger lithium domains and a higher lithium deposition density. These insights highlight how tailored interfacial chemistry, characterized by an inorganic -rich SEI, regulates lithium nucleation and growth, thereby contributing to improved cycling stability in anode-free cells.

To further elucidate the improved cycling performance in the narrower voltage window, the morphologies of cycled anodes and NCA cathodes were compared after 100 cycles in 3.6–4.3 V and 3.0–4.5 V windows (Figures S36–S38). Pronounced morphological differences are observed on the anode side, with more severe roughening and cracking under the wider 3.0-4.5 V window (Figures S38 and S39), whereas the cathode shows negligible morphological or cross-sectional degradation across voltage windows and cycling stages (Figures S37,S40 and S41). These results indicate (1) The capacity degradation in both voltage windows mainly stem from the lithium metal anode instead of cathode degradation. (2) The narrower voltage range improves the performance of the anode, and thus results in better cycling performance. Such conclusion is further supported by EIS results (Figure S17f), where the increase in charge-transfer resistance (ΔR_{ct}) after 100 cycles is much more pronounced on the anode side than on the cathode side for all electrolytes, indicating that interfacial degradation and impedance growth mainly originate from the anode side.

2.5 | Enhanced Thermal Stability With GPE-HFA

The combustion process in conventional electrolytes primarily originates from the generation of H· radicals via C—H bond cleavage at elevated temperatures, triggering chain combustion reactions [73, 74]. DFT calculations were conducted to quantitatively assess the capability of HFA molecules to scavenge H· radicals and thus function as effective flame retardants [75, 76]. Figure 5a and Figure S42 present the calculated binding energies (ΔE) for the reaction S + H· → S—H·, where S denotes the solvent molecules. Notably, HFA–H · exhibits the lowest binding energy of 0.36 eV, compared to DEC–H· (1.79 eV), FEC–H· (0.92 eV), and TMPTMA–H· (2.21 eV). This significantly lower ΔE highlights the superior H·radicals scavenging capability of the flame-retardant HFA additive, effectively enhancing its flame suppression performance during the combustion of electrolytes [77, 78]. To further investigate the flame-extinguishing effect of the GPE-HFA, its structural evolution under the action of oxygen in a high-temperature (1073 K) environment was simulated through ab initio molecular dynamics (AIMD) calculations [79]. After reaching a steady state at 5 ps, H· radicals formed in the gas-phase combustion chain become evident in the GPE (Figure 5d). In contrast, the F· radicals formed by GPE-HFA (Figure 5e) at high temperatures can effectively capture H· radicals, terminating their further propagation. Notably, the concentration of H·

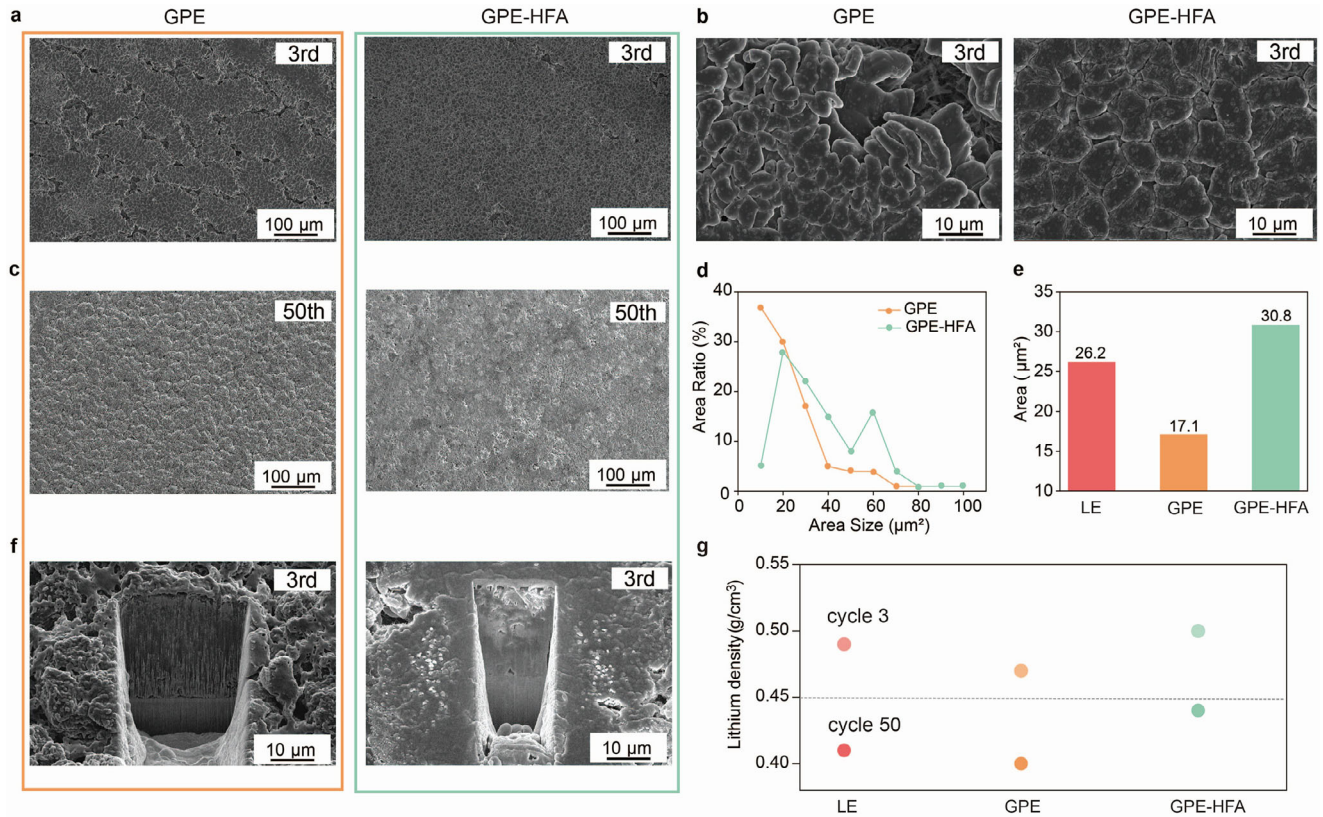

FIGURE 4 | (a,b) SEM images of lithium morphology deposited on Cu for GPE and GPE-HFA pouch cells, showing a more uniform deposition in GPE-HFA. Images were captured at the end of the charging of the 3rd cycle. (c) SEM images of lithium morphology deposited on Cu for GPE and GPE-HFA pouch cells, exhibiting a more compact deposition in GPE-HFA. Images were captured at the end of charging of the 50th cycle. (d) Lithium metal domain size distribution from cells with GPE and GPE-HFA (3rd cycle). (e) GPE-HFA shows the largest domain size compared with other electrolytes at the end of the 3rd cycle. (f) Electrode thickness of deposited lithium on Cu calculated from FIB-SEM results of GPE and GPE-HFA-based pouch cells (3rd cycle). (g) GPE-HFA shows the highest density of as-deposited lithium metal compared with other electrolytes after the 3rd charging and the 50th charging.

radicals in GPE-HFA decreases by 80.1% relative to that in GPE (Table S7).

The flame-retardant property of the HFA additive was first validated by experiments. As shown in Figure 5b,c, GPE readily ignites when exposed to a butane torch, whereas GPE-HFA remains non-flammable under exposure to the ignition source, demonstrating its superior flame resistance, even at a low concentration of 2.5 wt.%. Moreover, self-extinguishing time (SET) measurements were conducted to quantitatively evaluate the flammability of the electrolytes. 1 gram of electrolyte is used in the experiment. The GPE exhibits a high SET value of 58.6 s/g, indicative of severe and sustained combustion, whereas the GPE-HFA shows an SET of 0 s/g with no sustained burning after ignition. These results quantitatively confirm the markedly suppressed flammability and enhanced thermal stability enabled by HFA incorporation (Figure S43). In addition, the differential scanning calorimetry (DSC) shows that GPE-HFA generates ~27% less heat than GPE (Figure S44a), which shows enhanced thermal stability. The thermogravimetric analysis (TGA) also shows slightly slower mass loss in GPE-HFA than in GPE (Figure S44b). These results validate the advantage of GPE-HFA in terms of thermal stability.

To further validate the flame-retardant capability of GPE-HFA, drilling tests were conducted on multilayer Cu/NCA pouch cells. Remarkably, a 200 mAh Cu/NCA multilayer pouch cell-based GPE-HFA passes the harsh drilling test at the fully charged state (Video S1). During drilling, the central temperature only rises to ~47°C, and the cell voltage recovered upon drill removal (Figure 5i–k), highlighting the excellent thermal stability of GPE-HFA. In comparison, a 200 mAh Cu/NCA cell within GPE exploded during drilling with a central temperature > 100°C (Video S2), and the voltage dropped to 0 V after drilling (Figure 5f–h).

Impressively, even after 100 cycles, a fully charged 1.4 Ah cell-based GPE-HFA passes a drilling penetration test, reaching a peak central temperature of only 66°C and showing no signs of thermal runaway (Figure 5l–n and Video S3). In contrast to nail-penetration tests typically conducted after the first cycle, this evaluation was performed after 100 charge–discharge cycles at full state of charge, representing a substantially more stringent and practically relevant condition. Cycling-induced interfacial heterogeneity and inhomogeneous lithium deposition are known to accelerate parasitic reactions and compromise thermal stability [80, 81], thus increasing susceptibility to thermal runaway under mechanical abuse. The absence of thermal runaway under these ageing-aggravated conditions highlights the durability of the GPE-HFA system, which effectively mitigates lithium heterogeneity and side reactions over prolonged cycling. Moreover,

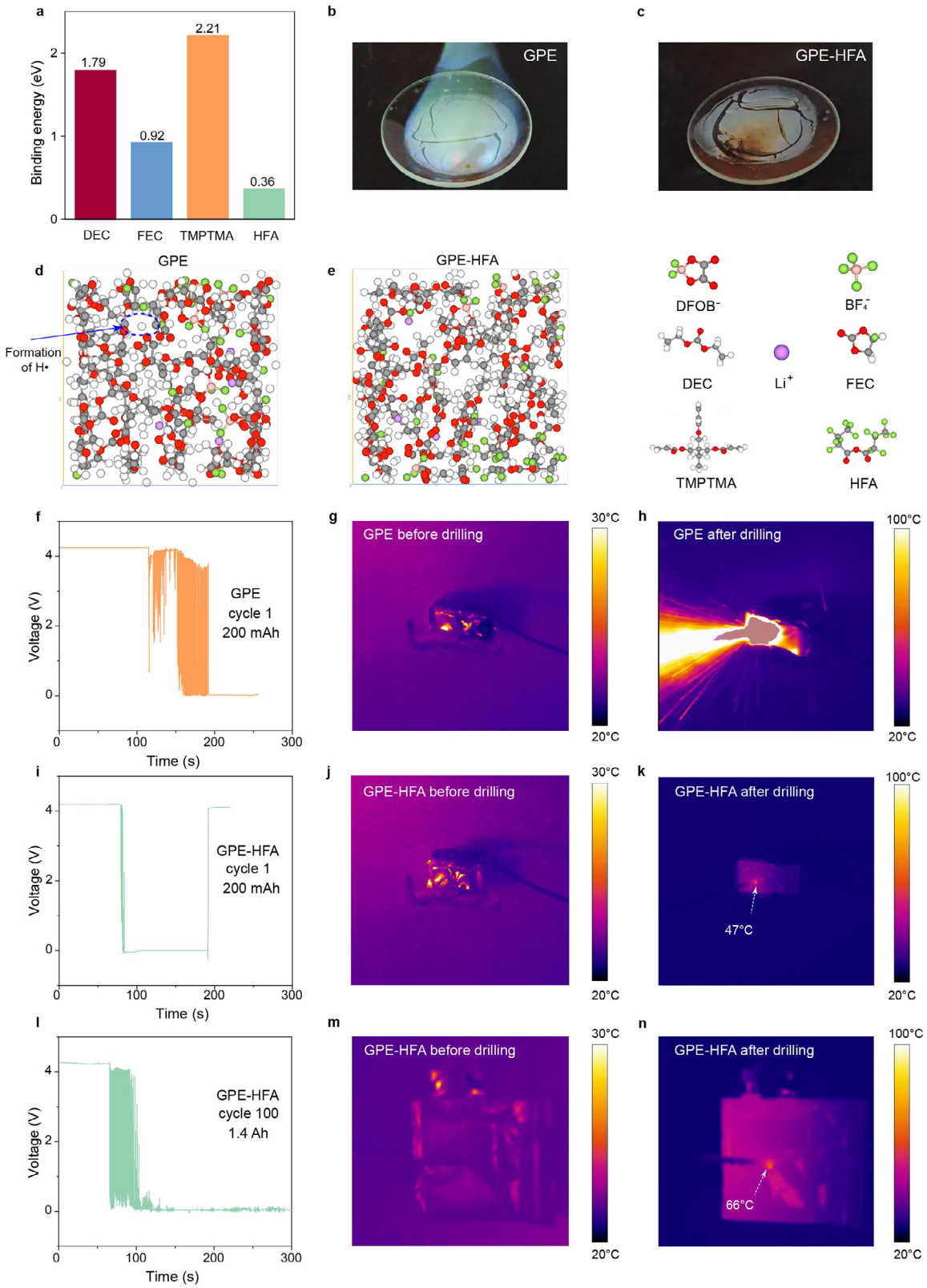

FIGURE 5 | (a) DFT calculations of binding energies of DEC−H·, FEC−H·, TMPTMA−H·, and HFA−H·. Combustion tests of (b) GPE and (c) GPE-HFA, demonstrate the enhanced thermal stability of GPE-HFA. (d,e) AIMD simulations of the structure evolutions of GPE and GPE-HFA under the action of oxygen at high temperature (1073 K). (f) Voltage profile of a GPE-based 200 mAh anode-free pouch cell during a drilling test. Infrared thermography images recorded before (g) and after (h) drilling, showing pronounced temperature rise and poor thermal stability. (i) Voltage profile of a GPE-HFA-based 200 mAh anode-free pouch cell during a drilling test. Corresponding infrared thermography images before (j) and after (k) drilling. GPE-HFA exhibits no thermal runaway in the drilling test. (l) Voltage profile of a GPE-HFA-based 1.4 Ah anode-free pouch cell after 100 cycles during a drilling test. Infrared thermography images before (m) and after (n) drilling. GPE-HFA shows impressive thermal stability even after 100 cycles.

such a pronounced difference in the safety test is also attributed to the ability of HFA to effectively scavenge solvent-derived H· radicals, thus significantly suppressing the flammability of GPE-HFA. Beyond drilling, the GPE-HFA-based 1.4 Ah pouch cell maintained stable power output even under mechanical abuse (Figures S45 and S46).

3 | Conclusion

We report a dual-functional fluorinated additive that enables in situ gelation, simultaneously delivering excellent cycling stability and enhanced safety in anode-free lithium-metal batteries. Through a cross-linking process, the GPE-HFA was precisely engineered with an optimized HFA concentration to tailor SEI composition, thereby achieving high anodic stability. Moreover, the strong free radical scavenging capability of HFA imparts flame-retardant properties, effectively mitigating thermal runaway risks in multilayer cells. Following this design, GPE-HFA exhibits significantly improved lithium deposition morphology and higher deposition density compared to the additive-free counterpart. Cryo-TEM and XPS analysis confirm the formation of a thin and inorganic-rich SEI containing LiF/Li_2O in GPE-HFA. Impressively, GPE-HFA-based Cu/NCA multilayer pouch cells with capacities of 1.4 Ah (3.0–4.5 V) and 200 mAh (3.6–4.3 V) retain 74.6% and 92.9% of their initial capacity after 100 cycles, respectively, when cycled at 0.5 C discharge. Such results are comparable to, or better than, the best performances reported to date. Moreover, such a 1.4 Ah Cu/NCA cell successfully passes the drilling test in the fully charged state even after 100 cycles. Overall, these findings demonstrate a viable strategy for constructing high-performance, safe anode-free lithium metal batteries, while the use of HFA as an additive offers mechanism insights into interfacial chemistry that can guide future electrolyte design.

Acknowledgements

Yuan Yang acknowledges support from the SAMSUNG SDI R&D Center in Suwon, and America.

Conflicts of Interest

The authors declare no conflicts of interest.

Data Availability Statement

The data that support the findings of this study are available from the corresponding author upon reasonable request.

References

1. Y. Qiao, H. Yang, Z. Chang, H. Deng, X. Li, and H. Zhou, "A High-Energy-Density and Long-Life Initial-Anode-Free Lithium Battery Enabled by a Li_2O Sacrificial Agent," *Nature Energy* 6 (2021): 653–662, https://doi.org/10.1038/s41560-021-00839-0.

2. R. Weber, M. Genovese, A. Louli, et al., "Long Cycle Life and Dendrite-Free Lithium Morphology in Anode-Free Lithium Pouch Cells Enabled by a Dual-Salt Liquid Electrolyte," *Nature Energy* 4 (2019): 683–689, https://doi.org/10.1038/s41560-019-0428-9.

3. T. Zhang, K. Huang, Y. Zheng, et al., "Loss and Recovery of Effective Lithium in Anode-Free Solid-State Lithium Metal Batteries," *Advanced Materials* 37 (2025): 05695, https://doi.org/10.1002/adma.202505695.

4. S. E. Sandoval, C. G. Haslam, B. S. Vishnugopi, et al., "Electro-Chemo-Mechanics of Anode-Free Solid-State Batteries," *Nature Materials* 24 (2025): 673–681, https://doi.org/10.1038/s41563-024-02055-z.

5. S. E. Sandoval, J. A. Lewis, B. S. Vishnugopi, et al., "Structural and Electrochemical Evolution of Alloy Interfacial Layers in Anode-Free Solid-State Batteries," *Joule* 7 (2023): 2054–2073, https://doi.org/10.1016/j.joule.2023.07.022.

6. M.-Y. Zhou, X.-Q. Ding, J.-F. Ding, et al., "Quantifying the Apparent Electron Transfer Number of Electrolyte Decomposition Reactions in Anode-Free Batteries," *Joule* 6 (2022): 2122–2137, https://doi.org/10.1016/j.joule.2022.07.003.

7. J. Wang, Y. Wang, X. Lu, et al., "Ultra-Sleek High Entropy Alloy Tights: Realizing Superior Cyclability for Anode-Free Battery," *Advanced Materials* 36 (2024): 2308257, https://doi.org/10.1002/adma.202308257.

8. A. Hu, W. Chen, F. Li, et al., "Nonflammable Polyfluorides-Anchored Quasi-Solid Electrolytes for Ultra-Safe Anode-Free Lithium Pouch Cells Without Thermal Runaway," *Advanced Materials* 35 (2023): 2304762, https://doi.org/10.1002/adma.202304762.

9. Y. An, Y. Zeng, D. Luan, and X. W. D. Lou, "Materials Design for High-Energy-Density Anode-Free Batteries," *Matter* 7 (2024): 1466–1502, https://doi.org/10.1016/j.matt.2024.02.012.

10. Q. Ma, J. Yue, M. Fan, et al., "Formulating the Electrolyte Towards High-Energy and Safe Rechargeable Lithium–Metal Batteries," *Angewandte Chemie International Edition* 60 (2021): 16554–16696, https://doi.org/10.1002/ange.202103850.

11. H. Wang, Z. Yu, X. Kong, et al., "Liquid Electrolyte: the Nexus of Practical Lithium Metal Batteries," *Joule* 6 (2022): 588–616, https://doi.org/10.1016/j.joule.2021.12.018.

12. B. Jiang, W. E. Gent, F. Mohr, et al., "Bayesian Learning for Rapid Prediction of Lithium-Ion Battery-Cycling Protocols," *Joule* 5 (2021): 3187–3203, https://doi.org/10.1016/j.joule.2021.10.010.

13. M. Zhou, R. Liu, D. Jia, et al., "Ultrathin Yet Robust Single Lithium-Ion Conducting Quasi-Solid-State Polymer-Brush Electrolytes Enable Ultralong-Life and Dendrite-Free Lithium-Metal Batteries," *Advanced Materials* 33 (2021): 2100943, https://doi.org/10.1002/adma.202100943.

14. Q. Liu, L. Wang, and X. He, "Toward Practical Solid-State Polymer Lithium Batteries by In Situ Polymerization Process: A Review," *Advanced Energy Materials* 13 (2023): 2300798, https://doi.org/10.1002/aenm.202300798.

15. D. Li, C. Xie, Y. Gao, H. Hu, L. Wang, and Z. Zheng, "Inverted Anode Structure for Long-Life Lithium Metal Batteries," *Advanced Energy Materials* 12 (2022): 2200584, https://doi.org/10.1002/aenm.202200584.

16. Q. K. Zhang, S. Y. Sun, M. Y. Zhou, et al., "Reforming the Uniformity of Solid Electrolyte Interphase by Nanoscale Structure Regulation for Stable Lithium Metal Batteries," *Angewandte Chemie International Edition* 62 (2023): 202306889, https://doi.org/10.1002/ange.202306889.

17. J. Weng, A. Jossen, A. Stefanopoulou, J. Li, X. Feng, and G. Offer, "Fast-Charging Lithium-Ion Batteries Require a Systems Engineering Approach," *Nature Energy* 10 (2025): 1289–1290, https://doi.org/10.1038/s41560-025-01813-w.

18. Z. Li, L. Wang, X. Huang, and X. He, "Unveiling the Mystery of LiF Within Solid Electrolyte Interphase in Lithium Batteries," *Small* 20 (2024): 2305429, https://doi.org/10.1002/smll.202305429.

19. H. Wan, J. Xu, and C. Wang, "Designing Electrolytes and Interphases for High-Energy Lithium Batteries," *Nature Reviews Chemistry* 8 (2024): 30–44, https://doi.org/10.1038/s41570-023-00557-z.

20. Y. Mu, Y. Chu, Y. Shi, et al., "Constructing Robust LiF-Enriched Interfaces in High-Voltage Solid-State Lithium Batteries Utilizing Tailored Oriented Ceramic Fiber Electrolytes," *Advanced Energy Materials* 14 (2024): 2400725, https://doi.org/10.1002/aenm.202400725.

21. Y. H. Tan, G. X. Lu, J. H. Zheng, et al., "Lithium Fluoride in Electrolyte for Stable and Safe Lithium-Metal Batteries," *Advanced Materials* 33 (2021): 2102134, https://doi.org/10.1002/adma.202102134.

22. W. Liang, X. Zhou, B. Zhang, et al., "The Versatile Establishment of Charge Storage in Polymer Solid Electrolyte With Enhanced Charge Transfer for LiF-Rich SEI Generation in Lithium Metal Batteries," *Angewandte Chemie International Edition* 63 (2024): 202320149, https://doi.org/10.1002/ange.202320149.

23. G. Jiang, F. Li, H. Wang, et al., "Perspective on High-Concentration Electrolytes for Lithium Metal Batteries," *Small Structures* 2 (2021): 2000122, https://doi.org/10.1002/sstr.202000122.

24. C. M. Efaw, Q. Wu, N. Gao, et al., "Localized High-Concentration Electrolytes Get More Localized Through Micelle-Like Structures," *Nature materials* 22 (2023): 1531–1539, https://doi.org/10.1038/s41563-023-01700-3.

25. X. Ren, L. Zou, X. Cao, et al., "Enabling High-Voltage Lithium-Metal Batteries Under Practical Conditions," *Joule* 3 (2019): 1662–1676, https://doi.org/10.1016/j.joule.2019.05.006.

26. X. Ren, S. Chen, H. Lee, et al., "Localized High-Concentration Sulfone Electrolytes for High-Efficiency Lithium-Metal Batteries," *Chem* 4 (2018): 1877–1892, https://doi.org/10.1016/j.chempr.2018.05.002.

27. P. Li, Z. Zhang, Z. Zhao, X. Zhang, H. Zhang, and G. Li, "Localized Medium Concentration Electrolyte With Fast Kinetics for Lithium Metal Batteries," *Angewandte Chemie International Edition* 63 (2024): 202319090, https://doi.org/10.1002/ange.202319090.

28. Y. Huang, R. Li, S. Weng, et al., "Eco-Friendly Electrolytes Via a Robust Bond Design for High-Energy Li Metal Batteries," *Energy & Environmental Science* 15 (2022): 4349–4361, https://doi.org/10.1039/d2ee01756c.

29. C. Zhang, S. Gu, D. Zhang, et al., "Nonflammable, Localized High-Concentration Electrolyte Towards a High-Safety Lithium Metal Battery," *Energy Storage Materials* 52 (2022): 355–364, https://doi.org/10.1016/j.ensm.2022.08.018.

30. Z. Cui, Z. Jia, D. Ruan, et al., "Molecular Anchoring of Free Solvents for High-Voltage and High-Safety Lithium Metal Batteries," *Nature Communications* 15 (2024): 2033, https://doi.org/10.1038/s41467-024-46186-y.

31. H. Zhang, G. G. Eshetu, X. Judez, C. Li, L. M. Rodriguez-Martínez, and M. Armand, "Electrolyte Additives for Lithium Metal Anodes and Rechargeable Lithium Metal Batteries: Progress and Perspectives," *Angewandte Chemie International Edition* 57 (2018): 15002–15027, https://doi.org/10.1002/anie.201712702.

32. J. Zheng, M. H. Engelhard, D. Mei, et al., "Electrolyte Additive Enabled Fast Charging and Stable Cycling Lithium Metal Batteries," *Nature Energy* 2 (2017): 17012, https://doi.org/10.1038/nenergy.2017.12.

33. T. M. Hagos, H. K. Bezabh, C.-J. Huang, S.-K. Jiang, W.-N. Su, and B. J. Hwang, "A Powerful Protocol Based on Anode-Free Cells Combined With Various Analytical Techniques," *Accounts of Chemical Research* 54 (2021): 4474–4485, https://doi.org/10.1021/acs.accounts.1c00528.

34. X. Meng, Y. Liu, M. Guan, J. Qiu, and Z. Wang, "A High-Energy and Safe Lithium Battery Enabled by Solid-State Redox Chemistry in a Fireproof Gel Electrolyte," *Advanced Materials* 34 (2022): 2201981, https://doi.org/10.1002/adma.202201981.

35. J. Castillo, A. Santiago, X. Judez, et al., "Safe, Flexible, and High-Performing Gel-Polymer Electrolyte for Rechargeable Lithium Metal Batteries," *Chemistry of Materials* 33 (2021): 8812–8821, https://doi.org/10.1021/acs.chemmater.1c02952.

36. C. Zhang, Z. Lu, M. Song, et al., "Highly Oxidation-Resistant Ether Gel Electrolytes for 4.7 V High-Safety Lithium Metal Batteries," *Advanced Energy Materials* 13 (2023): 2203870, https://doi.org/10.1002/aenm.202203870.

37. S. Ma, J. Zhao, H. Xiao, et al., "Modulating the Inner Helmholtz Plane Towards Stable Solid Electrolyte Interphase by Anion-Π Interactions for High-Performance Anode-Free Lithium Metal Batteries," *Angewandte Chemie International Edition* 137 (2025): 202412955, https://doi.org/10.1002/ange.202412955.

38. I. R. Choi, Y. Chen, A. Shah, et al., "Asymmetric Ether Solvents for High-Rate Lithium Metal Batteries," *Nature Energy* 10 (2025): 365–379, https://doi.org/10.1038/s41560-025-01716-w.

39. J. Lee, J. Kim, W. Jang, et al., "A Strategic Tuning of Interfacial Li^+ Solvation With Ultrathin Polymer Layers for Anode-Free Lithium Metal Batteries," *Joule* 10 (2025): 102226, https://doi.org/10.1016/j.joule.2025.102226.

40. D. Y. Han, S. Kim, J. Son, et al., "Synergistic Coupling of Host and Electrolyte Achieving 1270 Wh L^{-1} in Anode-Free Lithium Metal Batteries," *Advanced Materials* 38 (2025): 15906, https://doi.org/10.1002/adma.202515906.

41. L. Liu, Y. Xiang, and J. Wang, "From Cell to Atomic Level: Understanding the Degradation in 99% Coulombic Efficiency and 450 Wh Kg^{-1} Anode-Free Pouch Cells," *Journal of the American Chemical Society* 147 (2025): 41342–41354, https://doi.org/10.1021/jacs.5c09562.

42. M. Mao, L. Gong, X. Wang, et al., "Electrolyte Design Combining Fluoro-With Cyano-Substitution Solvents for Anode-Free Li Metal Batteries," *Proceedings of the National Academy of Sciences* 121 (2024): 2316212121, https://doi.org/10.1073/pnas.2316212121.

43. J. Shi, T. Koketsu, Z. Zhu, et al., "In Situ P-Block Protective Layer Plating in Carbonate-Based Electrolytes Enables Stable Cell Cycling in Anode-Free Lithium Batteries," *Nature Materials* 23 (2024): 1686–1694, https://doi.org/10.1038/s41563-024-01997-8.

44. C. Gervillie-Mouravieff, L. Ah, A. Liu, C.-J. Huang, and Y. S. Meng, "Deciphering the Impact of the Active Lithium Reservoir in Anode-Free Pouch Cells," *ACS Energy Letters* 9 (2024): 1693–1700, https://doi.org/10.1021/acsenergylett.4c00457.

45. M. Mao, X. Ji, Q. Wang, et al., "Anion-Enrichment Interface Enables High-Voltage Anode-Free Lithium Metal Batteries," *Nature communications* 14 (2023): 1082, https://doi.org/10.1038/s41467-023-36853-x.

46. Z. Zhang, H. Luo, Z. Liu, S. Wang, X. Zhou, and Z. Liu, "A Chemical Lithiation Induced $Li_{4.4}Sn$ Lithiophilic Layer for Anode-Free Lithium Metal Batteries," *Journal of Materials Chemistry A* 10 (2022): 9670–9679, https://doi.org/10.1039/d2ta00167e.

47. S. Zhang, R. Li, N. Hu, et al., "Tackling Realistic Li^+ Flux for High-Energy Lithium Metal Batteries," *Nature communications* 13 (2022): 5431, https://doi.org/10.1038/s41467-022-33151-w.

48. L. Lin, L. Suo, Y. S. Hu, H. Li, X. Huang, and L. Chen, "Epitaxial Induced Plating Current-Collector Lasting Lifespan of Anode-Free Lithium Metal Battery," *Advanced Energy Materials* 11 (2021): 2003709, https://doi.org/10.1002/aenm.202003709.

49. C. Niu, D. Liu, J. A. Lochala, et al., "Balancing Interfacial Reactions to Achieve Long Cycle Life in High-Energy Lithium Metal Batteries," *Nature Energy* 6 (2021): 723–732, https://doi.org/10.1038/s41560-021-00852-3.

50. L. Lin, K. Qin, Q. Zhang, et al., "Li-Rich $Li_2[Ni_{0.8}Co_{0.1}Mn_{0.1}]O_2$ for Anode-Free Lithium Metal Batteries," *Angewandte Chemie International Edition* 60 (2021): 8289–8296, https://doi.org/10.1002/anie.202017063.

51. F. Liu, J. Wang, W. Chen, et al., "Polymer-Ion Interaction Prompted Quasi-Solid Electrolyte for Room-Temperature High-Performance Lithium-Ion Batteries," *Advanced Materials* 36 (2024): 2409838, https://doi.org/10.1002/adma.202409838.

52. Z. Xu, C. Lin, J. Qiu, and Z. Wang, "Polymer-Regulated Solvation and Interphase Engineering for Long-Life and Safe Quasi-Solid-State Anode-Free Sodium Batteries," *Advanced Materials* 37 (2025): 2506037, https://doi.org/10.1002/adma.202506037.

53. G. Singer, C. T. Hsieh, T. Jin, S. H. Lee, and Y. Yang, "A Quasi-Solid Polymer Electrolyte-Based Structural Battery With High Mechanical and Electrochemical Performance," *EcoMat* 5 (2023): 12418, https://doi.org/10.1002/eom2.12418.

54. S. Cong, Z. Yang, X. Wan, et al., "Gel Electrolyte Featuring Parasitic Salt-Phobic Network Enables Anode-Free Lithium Batteries With Long Cycle Life and Enhanced Thermal Stability," *Joule* 10 (2026): 102293, https://doi.org/10.1016/j.joule.2025.102296.

55. A. Louli, A. Eldesoky, R. Weber, et al., "Diagnosing and Correcting Anode-Free Cell Failure Via Electrolyte and Morphological Analysis," *Nature Energy* 5 (2020): 693–702, https://doi.org/10.1038/s41560-020-0668-8.

56. Y. Wang, L. Ren, Q. Zhang, et al., "Fluorine-Rich Electrolyte Additive for Achieving Dendrite-Free Lithium Anodes at Low Temperatures," *ACS Applied Materials & Interfaces* 16 (2024): 47674–47682, https://doi.org/10.1021/acsami.4c10028.

57. L. Zhang, M. Bai, X. Wang, Z. Huang, B. Hong, and Y. Lai, "A Strong Nucleophilic Fluorination Agent to Achieve Highly Stable In-Situ 3D Cross-Linked Gel Polymer Electrolyte for Lithium-Ion Batteries," *Chemical Engineering Journal* 481 (2024): 148579, https://doi.org/10.1016/j.cej.2024.148579.

58. S. Li, W. Zhang, Q. Wu, et al., "Synergistic Dual-Additive Electrolyte Enables Practical Lithium-Metal Batteries," *Angewandte Chemie International Edition* 59 (2020): 14935–14941.

59. P. Bai, X. Ji, J. Zhang, et al., "Formation of LiF-Rich Cathode-Electrolyte Interphase by Electrolyte Reduction," *Angewandte Chemie International Edition* 61 (2022): 202202731, https://doi.org/10.1002/anie.202202731.

60. G. Ye, X. Hong, M. He, et al., "All-Solid-State Lithium Metal Batteries With Microdomain-Regulated Polycationic Solid Electrolytes," *Advanced Materials* 37 (2025): 2417829, https://doi.org/10.1002/adma.202417829.

61. H. Wang, M. Wu, J. He, et al., "Highly Li^+ Conductive Artificial Solid Electrolyte Interphase for Lithium Metal Batteries," *Energy Material Advances* 6 (2025): 0105, https://doi.org/10.34133/energymatadv.0105.

62. B. D. Adams, J. Zheng, X. Ren, W. Xu, and J. G. Zhang, "Accurate Determination of Coulombic Efficiency for Lithium Metal Anodes and Lithium Metal Batteries," *Advanced Energy Materials* 8 (2018): 1702097, https://doi.org/10.1002/aenm.201702097.

63. X. Ma, D. Zhang, H. Fu, et al., "Energy Band-Engineered Solid Electrolyte Interphase for Stable Potassium-Ion Batteries," *Joule* 9 (2025): 101952, https://doi.org/10.1016/j.joule.2025.101952.

64. U.-H. Kim, S.-B. Lee, N.-Y. Park, S. J. Kim, C. S. Yoon, and Y.-K. Sun, "High-Energy-Density Li-Ion Battery Reaching Full Charge in 12 min," *ACS Energy Letters* 7 (2022): 3880–3888, https://doi.org/10.1021/acsenergylett.2c02032.

65. T. Yim, K. Kim, M. Q. Hassig, et al., "Lithium-Nitrate-Containing Gel Polymer Electrolyte for Carbonate-Based Anode-Free Lithium Metal Batteries," *ACS applied materials & interfaces* 17 (2025): 37851–37862, https://doi.org/10.1021/acsami.5c03252.

66. T. Agnihotri, S. A. Ahmed, E. B. Tamilarasan, et al., "Anion-Trapping Composite Gel Electrolyte for Safer and More Stable Anode-Free Lithium-Metal Batteries," *Chemical Engineering Journal* 484 (2024): 149608, https://doi.org/10.1016/j.cej.2024.149608.

67. Y.-H. Lin, L.-T. Wu, Y.-T. Zhan, et al., "Self-Assembly Formation of Solid-Electrolyte Interphase in Gel Polymer Electrolytes for High Performance Lithium Metal Batteries," *Energy Storage Materials* 61 (2023): 102868, https://doi.org/10.1016/j.ensm.2023.102868.

68. R. Tian, S.-H. Park, P. J. King, et al., "Quantifying the Factors Limiting Rate Performance in Battery Electrodes," *Nature communications* 10 (2019): 1933, https://doi.org/10.1038/s41467-019-09792-9.

69. Y. Li, Y. Li, A. Pei, et al., "Atomic Structure of Sensitive Battery Materials and Interfaces Revealed by Cryo–Electron Microscopy," *Science* 358 (2017): 506–510, https://doi.org/10.1126/science.aam6014.

70. Z. Zhang, Y. Li, R. Xu, et al., "Capturing the Swelling of Solid-Electrolyte Interphase in Lithium Metal Batteries," *Science* 375 (2022): 66–70, https://doi.org/10.1126/science.abi8703.

71. H. Zhu, Q. Zhang, K. Wang, et al., "Minimizing Solvent-Coordination in Ether Electrolytes for Lithium Metal Batteries Under Extreme Operating Conditions," *Advanced Materials* 37 (2025): 2505892, https://doi.org/10.1002/adma.202505892.

72. X. Hu, S. Shen, J. Li, et al., "Modulating Physicochemical Interfaces Enables Li-Rich Oxides Based Ceramic Solid-State Li Batteries Under Ambient Conditions," *Nature Communications* 16 (2025): 9338, https://doi.org/10.1038/s41467-025-64396-w.

73. S. Zhang, S. Li, and Y. Lu, "Designing Safer Lithium-Based Batteries With Nonflammable Electrolytes: A Review," *eScience* 1 (2021): 163–177, https://doi.org/10.1016/j.esci.2021.12.003.

74. C. Zu, H. Yu, and H. Li, "Enabling the Thermal Stability of Solid Electrolyte Interphase in Li-Ion Battery," *InfoMat* 3 (2021): 648–661, https://doi.org/10.1002/inf2.12190.

75. Y. Zhu, X. Luo, H. Zhi, et al., "Diethyl (Thiophen-2-Ylmethyl) Phosphonate: A Novel Multifunctional Electrolyte Additive for High Voltage Batteries," *Journal of materials chemistry A* 6 (2018): 10990–11004, https://doi.org/10.1039/c8ta01236a.

76. Q. Zhang, S. Liu, Z. Lin, et al., "Highly Safe and Cyclable Li-Metal Batteries With Vinylethylene Carbonate Electrolyte," *Nano Energy* 74 (2020): 104860, https://doi.org/10.1016/j.nanoen.2020.104860.

77. P. Jaumaux, J. Wu, D. Shanmukaraj, et al., "Non-Flammable Liquid and Quasi-Solid Electrolytes Toward Highly-Safe Alkali Metal-Based Batteries," *Advanced Functional Materials* 31 (2021): 2008644, https://doi.org/10.1002/adfm.202008644.

78. J. Xiang, Y. Zhang, B. Zhang, et al., "A Flame-Retardant Polymer Electrolyte for High Performance Lithium Metal Batteries With an Expanded Operation Temperature," *Energy & Environmental Science* 14 (2021): 3510–3521, https://doi.org/10.1039/d1ee00049g.

79. Y. Sun, T. Yang, H. Ji, et al., "Boosting the Optimization of Lithium Metal Batteries by Molecular Dynamics Simulations: A Perspective," *Advanced Energy Materials* 10 (2020): 2002373, https://doi.org/10.1002/aenm.202002373.

80. J. Kim, W. Lee, J. Seok, et al., "Electrochemical Profiling Method for Diagnosis of Inhomogeneous Reactions in Lithium-Ion Batteries," *Cell Reports Physical Science* 4 (2023): 101331, https://doi.org/10.1016/j.xcrp.2023.101331.

81. H. Zhou, C. Fear, R. E. Carter, C. T. Love, and P. P. Mukherjee, "Correlating Lithium Plating Quantification With Thermal Safety Characteristics of Lithium-Ion Batteries," *Energy Storage Materials* 66 (2024): 103214, https://doi.org/10.1016/j.ensm.2024.103214.

Supporting Information

Additional supporting information can be found online in the Supporting Information section.

Supporting File 1: adma74069-sup-0001-SuppMat.docx.

Supporting File 2: adma74069-sup-0002-VideoS1.mp4.

Supporting File 3: adma74069-sup-0003-VideoS2.mp4.

Supporting File 4: adma74069-sup-0004-VideoS3.mp4.